Lasers in Manufacturing Conference 2021

Laser-based powder bed fusion with 16 kW

Artur Leis[a,b,*], Stefan Bechler[b], Rudolf Weber[b], Thomas Graf[b]

[a]*Graduate School of Excellence advanced Manufacturing Engineering (GSaME), Nobelstraße 12, 70569 Stuttgart, Germany*
[b]*Institut für Strahlwerkzeuge (IFSW), Pfaffenwaldring 43, 70569 Stuttgart, Germany*

Abstract

Laser-based Powder Bed Fusion (LPBF) is typically performed at laser powers between 500 - 1000 W, and diameters of the laser beam between 50 µm - 500 µm. As the build rate is directly connected with the applied laser power, a reduction of the process time requires an increase of the applied laser power. In order to build large parts in a sufficient time, the implementation of high laser powers in LBPF is of high interest.
To increase the build rate, the laser power was set to be 16 kW and the diameter of the laser beam was determined to generate continuous melt beads. Additively manufactured samples of AlSi10Mg were used for the high-power experiments. The melting process was recorded with a high-speed camera. The generated beads were analysed metallographically to determine the extent and shape of the molten region and the porosity.
Diameters of the laser beam between 2.5 - 3.8 mm, feed rates within a range of 0.5 - 1.5 m/s lead at the laser power of 16 kW to continuous melt beads but show also strong hydrogen-induced porosity.

Keywords: laser-based powder bed fusion; high power; additive manufacturung; hydrogen; porosity

1. Introduction

Laser-based Powder Bed Fusion (LPBF) allows the generation of highly complex parts. Subsequent powder layers are molten with a laser beam, which has a typical diameter of the laser beam d_b of 50 - 500 µm. The small diameter of the laser beam d_b leads to the requirement of a large number of single adjacent melt beads for the formation of one layer. In order to avoid vaporization, the small diameter of the laser beam d_b allows only for low laser powers of <1000 W, which result in a build rate between 1.4 mm³/s and 50 mm³/s as summarized by Khorasani et al., 2020. These limitations of the build rate result from the material per time,

* Corresponding author. Tel.: +49 711 685 60428; fax: +49 711 685 66842
E-mail address: artur.leis@ifsw.uni-stuttgart.de

which can be molten with the given laser power as described by Hügel and Graf, 2014. One approach to increase the build rate is to increase the number of laser beams to enable parallelization, which was previously published by Khorasani et al., 2020; Sing and Yeong, 2020; Wong et al., 2019. In order to scale the build rate for a single laser beam, the high-power LPBF process with laser power of 16 kW is conducted in the following.

2. Experimental setup and evaluation procedure

Fig. 1 shows a schematic illustration of the experimental setup. A model arrangement was used for the investigation of the scalability of the laser power for the LPBF-process. A TruDisk16002 was used as laser source and the laser beam was delivered through a fiber with a core diameter of 600 µm to the processing optics. The magnification of the processing optics was 1, resulting in a focal diameter of 600 µm and a Rayleigh length of z_R = 3.11 mm. The laser optics was inclined opposite to the feed direction by 10° with respect to the normal of the surface of the sample and the laser beam was focused 13.7 - 17.8 mm below the surface of the samples to achieve diameters of the laser beam d_b of 2.52 - 3.27 mm on the surface of the sample. A simplified powder bed was used to manually apply new powder layers on previously additively manufactured samples, as shown in Fig. 1. Each powder layer provides a thickness to 250 µm. The sample was moved linearly in x-direction with feed rates of 0.5 m/s, 1 m/s, and 1.5 m/s. In order to capture the process with a high-speed camera at frame rates of 8,000 fps and illumination times of 90-100 µs, a diode laser with a wavelength of 808 nm illuminated the process area. Nitrogen was applied as shielding gas during the process.

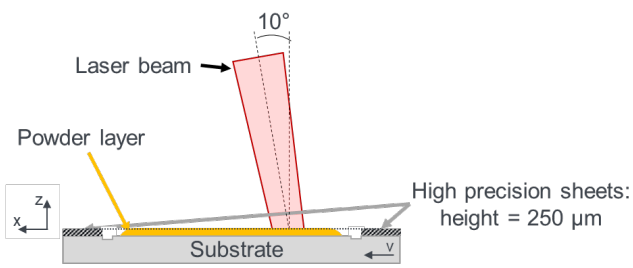

Fig. 1. Schematic illustration of the experimental setup with inclined laser beam by 10° with respect to the normal of the surface of the sample and applied powder layer on the surface of the sample.

In order to generate continuous melt beads with the full laser power of 16 kW, the diameter of the laser beam d_b was varied by changing the focal position z to decrease the distance between laser optics and sample. Table 1 lists the applied parameter combinations for the experiments. The diameter of the laser beam d_b of the defocused beam on the surface of the sample was determined with a Primes FocusMonitor by a measurement of the laser beam caustic.

Table 1. Parameter used for the experiments

Feed rate v in m/s	0.5	1.0	1.5
Laser power P_L in kW	16		
Thickness of the powder layer in µm	250		
Diameter of the laser beam d_b in mm	$2.52 < d_b < 3.27$		

Fig. 2 shows a microscope picture of the cross-section of a solidified melt bead. The productivity per power of the incident laser beam

$$\dot{\Upsilon}_P = \frac{A_a \cdot v}{P_L}, \tag{1}$$

results from the product of the measured cross-sectional area of the added material A_a and the feed rate v in relation to the incident laser power P_L. The build rate

$$\dot{V} = A_a \cdot v, \tag{2}$$

results from the product of the measured cross-sectional area of the added material A_a and the feed rate v.

The cross-sectional area of the added material A_a is represented by the red line in the example of Fig. 2. Pores are highlighted by green circles in Fig. 2 and the relative porosity

$$\xi = \frac{\sum A_P}{A_a}, \tag{3}$$

was determined by their complete area in the cross section $\sum A_P$ in relation to the cross-sectional area A_a of the added material, as defined in VDI-3405, 2016.

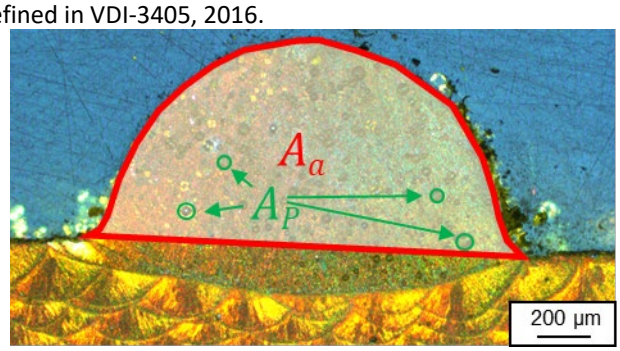

Fig. 2. Image of a cross-section of a sample with a generated and solidified melt bead. The red line marks the cross-sectional area of the added material A_a. The green line marks the cross-sectional areas A_P of exemplary pores.

The results of the performed experiments for high-power LPBF are represented as functions of the diffusion length l_{th}

$$l_{th} = 2 \cdot \sqrt{\frac{\lambda}{\rho \cdot c_P} \cdot t}, \tag{4}$$

where λ is the heat-conduction of the material, ρ is the density of the bulk material, c_P is the heat capacity of the material, and the time of irradiation per volume element

$$t = \frac{d_b}{v} \tag{5}$$

for a moving heat source on the surface, as described by Arata et al., 1978, where d_b is the diameter of the laser beam on the surface of the sample and v is the feed rate of the moving sample. Table 2 lists the material properties for AlSi10Mg, which were used for the calculation of the diffusion length l_{th}.

Table 2. Material properties for AlSi10Mg provided by the datasheet of Raffmetal S.p.a.

λ in $\frac{\mathrm{W}}{\mathrm{m \cdot K}}$	ρ in $\frac{\mathrm{kg}}{\mathrm{m^3}}$	c_P in $\frac{\mathrm{J}}{\mathrm{kg \cdot K}}$
150	2680	910

3. Results

Fig. 3 a) represents the productivity $\dot{Y}_P$ as a function of the diffusion length l_{th} for processes with diameters of the laser beam d_b in the range of 2.52 mm and 3.27 mm, which do not show spatter formation or balling. The value illustrated by the yellow circle represents the productivity $\dot{Y}_P$, which is realised with current LPBF-machines as summarised by Khorasani et al., 2020. The measurements illustrated by the square represent the results of the experiments carried out with 16 kW and a feed rate v of 1.5 m/s (green), 1 m/s (red), and 0.5 m/s (blue). The productivity $\dot{Y}_P$ for high-power LPBF is as in the same range of 0.04±0.02 mm³/s/W as for the state of the art LPBF-machines with conventional process parameters. Fig. 3 b) represents the build rate $\dot{V}$ as a function of the diffusion length l_{th}. The value illustrated by the yellow circle represents the build rate $\dot{V}$, which is realised with current LPBF-machines as summarized by Khorasani et al., 2020. The measurements illustrated by the square represent the results of the experiments carried out with 16 kW and a feed rate v of 1.5 m/s (green), 1 m/s (red), and 0.5 m/s (blue). This proves, that that the build rate $\dot{V}$ is proportional to the incident laser power P_L.

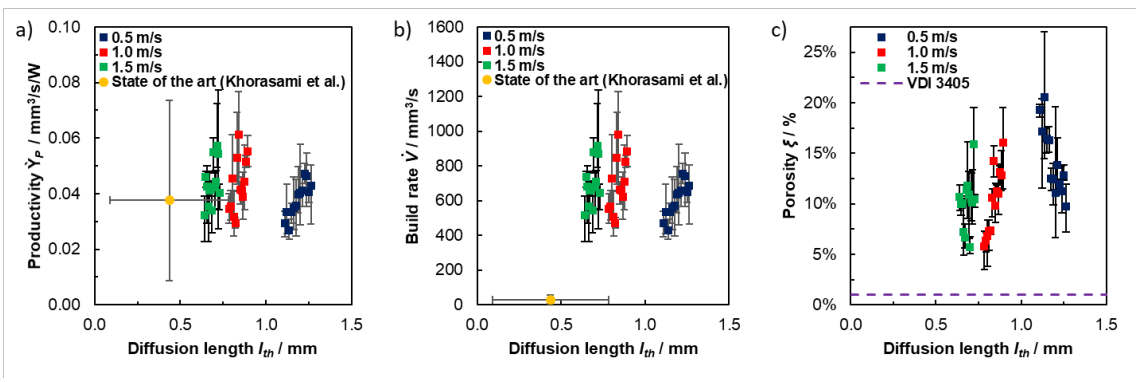

Fig. 3. (a) productivity $\dot{Y}_P$ in mm³/s/W as a function of the diffusion length l_{th} in mm; (b) build rate $\dot{V}$ in mm³/s as a function of the diffusion length l_{th} in mm; (c) porosity ξ in % as a function of the diffusion length l_{th} in mm.

The productivity $\dot{Y}_P$ for high-power LPBF is in the same range as for current LPBF-machines and as we use more power, the build rate $\dot{V}$ is significantly increased.

In Fig. 3 c) the porosity ξ of the generated melt beads is shown as a function of the diffusion length l_{th}. The violet dashed line describes the tolerated porosity of 1% for parts produced by means of LPBF as it is defined in VDI-3405, 2016. The measurements illustrated by the square represent the results of the experiments carried out with 16 kW and a feed rate v of 1.5 m/s (green), 1 m/s (red), and 0.5 m/s (blue). The solidified melt beads show a significant increase of the porosity through all measurements with values between 3% and 25%. The degassing effect as described by Weingarten et al., 2015, after a heat treatment at 550°C for 60 min proves that the pores are hydrogen induced.

4. Conclusion

The productivity per power of the incident laser beam $\dot{Y}_P$ at high-power LPBF is equal to the state of the art LPBF-machines. From this, one can conclude that the build rate $\dot{V}$ for the generation of a part is proportional to the incident laser power. A higher laser power allows for an increase of the build rate $\dot{V}$ in LPBF by the factor of 10-40 compared to conventional LPBF-processes. However, the hydrogen-induced porosity was increased significantly, which shows the need of further investigation.

References

Khorasani A., Gibson I., Veetil J. K., Ghasemi A. H., 2020. A review of technological improvements in laser-based powder bed fusion of metal printers. Int J Adv Manuf Technol 108, pp 191–209. doi: 10.1007/s00170-020-05361-3

Hügel H., Graf T. (2014). Laser in der Fertigung: Grundlagen der Strahlquellen, Systeme, Fertigungsverfahren, 3., überarb. u. erw. Aufl. Lehrbuch. Springer, Wiesbaden

Sing S. L., Yeong W. Y., 2020. Laser powder bed fusion for metal additive manufacturing: perspectives on recent developments. Virtual and Physical Prototyping 15, pp 359–370. doi: 10.1080/17452759.2020.1779999

Wong H., Dawson K., Ravi G. A., Howlett L., Jones R. O., Sutcliffe C. J., 2019. Multi-Laser Powder Bed Fusion Benchmarking—Initial Trials with Inconel 625. Int J Adv Manuf Technol 105, pp 2891–2906. doi: 10.1007/s00170-019-04417-3

VDI-3405, 2016. VDI-Richtlinie 3405 Part 2. VDI, Berlin

Arata Y, Maruo H, Miyamoto I, 1978. Application of Laser for Material Processing-Heat Flow in Laser Hardening-, IIW Doc

Raffmetal S.p.a. Leghe di alluminio in colata. Continuous casting aluminium alloys: AlSi10Mg. http://www.raffmetal.com/scarica_file.asp?c=/dati/SearchAlloy/ENG/&f=EN43000.pdf. Accessed 18 February 2020

Weingarten C., Buchbinder D., Pirch N., Meiners W., Wissenbach K., Poprawe R., 2015. Formation and reduction of hydrogen porosity during selective laser melting of AlSi10Mg. Journal of Materials Processing Technology 221, pp 112–120. doi: 10.1016/j.jmatprotec.2015.02.013